Metallography, Microstructure, and Analysis (2024) 13:1140–1152
https://doi.org/10.1007/s13632-024-01142-6

ORIGINAL RESEARCH ARTICLE

The Role of Niobium during Heat Treatment of High-Vanadium High-Speed Steel Rolls for Improved Mechanical Properties

Rivoningo E. Chauke[1] · Charles W. Siyasiya[1] · Davisn Nyabadza[1]

Received: 26 April 2024 / Revised: 8 September 2024 / Accepted: 25 September 2024 / Published online: 17 October 2024

Abstract

High-speed steel (HSS) provides superior wear resistance and high surface quality of rolled-steel products. In this study, the influence of niobium addition on the solidification behavior and microstructure of high-speed steel rolls and their impact on the roll's hardness and wear resistance were investigated by a combination of thermodynamic simulations of solidification using ThermoCalc, optical and scanning microscopy and hardness testing. The study was conducted on two centrifugal-cast commercial high-vanadium high-speed steel sleeves whose compositions differed in niobium content. Thermodynamic simulations showed that niobium promotes the precipitation of proeutectic Nb-rich MC carbide during solidification. Microscopic observations showed that the proeutectic carbide promotes carbide dispersion in the microstructure. This was found to improve the microhardness of the martensitic matrix and counteract softening during repeated tempering treatment. The addition of less than 2 wt.% Nb in the HSS roll yielded better hot hardness as a result of the roll's better microstructural integrity and response to HT. The conclusion was that Nb-containing HSS rolls can be produced for the hot-rolling stands that operate at higher rolling force and temperature if the cost-benefit analysis is favorable.

Keywords High-speed steel rolls · Solidification behavior · Eutectic carbides · Retained austenite

Introduction

Many commercial steels require hot-rolling before they can be made suitable for their specific engineering applications. Advanced hot strip mills (HSM) can expand the range of their hot-rolled-steel products to include much harder steels by using rolls with higher hot hardness and improved wear resistance. Owing to its superiority in these properties, high-speed steel (HSS) is currently one of the very few if not the only available commercial steel roll grades that allows for hot-rolling of flat steel products over a wider hardness range.

Until the beginning of the 1990 s, the finishing stands of HSM were dominated by high chrome (HiCr) and indefinite chill (IC) cast iron rolls [1–3]. These have since become less attractive as the demand for higher roll performance and high surface quality of rolled-steel products keeps increasing. HSS roll became the answer to most of these demands as it offers a better combination of surface roughness (which is the lowest) and oxide scale stability than the former [4, 5].

The HSS's superior wear resistance is attributed to the higher hot hardness, which is imparted by the hard alloy carbides in its microstructure. Its design is characterized by a particular combination of chemical composition and heat treatment (HT), tailored to attain a wide range of hardness and toughness. The main alloying elements include carbon, chromium, vanadium, molybdenum, and tungsten [3–6]. These elements are strong carbide formers, and therefore, precipitate hard carbides through eutectic and solid-state reactions during solidification and HT [3–6]. The most common carbides include the MC, M_7C_3, M_2C, and M_6C, where "M" refers to carbide-forming elements in solid solution [3–6].

A lot has been achieved in the development of the HSS roll, where it was also learned that both hot hardness and wear resistance can be improved further by improving carbide distribution in the microstructure. The focus has been to reduce the cell boundary carbide network consisting of M_7C_3 and M_2C and refine and disperse the MC carbide particles [7, 8]. To achieve this, several techniques, including electromagnetic centrifugal casting, variable solidification cooling

✉ Rivoningo E. Chauke
u27350097@tuks.co.za

[1] Department of Materials Science and Metallurgical Engineering, University of Pretoria, Pretoria, South Africa

rate and alloy compositional modifications, are currently being tried and employed [7–10]. In the latest advances, it has been found that additions of niobium, which has similar effects as vanadium, may enhance the hot hardness by refining the carbide particles and improving dispersion [5, 7]. Niobium also precipitates the MC carbide. However, it cannot be added as a complete substitute for vanadium because NbC starts to precipitate very early from the melt due to its very low Gibbs free energy, and may become very coarse during casting [11, 12]. The addition of niobium was also found to effectively decrease the solubility of vanadium and molybdenum in the MC carbide [13]. Kim et al. [6] also showed that niobium addition increased both vanadium and molybdenum in solid solution of the austenite during solidification. Ultimately, these elements enhance the solid-state precipitation of the submicron-size vanadium-rich MC carbide particles in the austenitic matrix, thereby improving the matrix hardness [6]. As much as 1.5 wt.% Nb can be added to the HSS alloy with hardness improvement [6].

During casting, the solidification of the sleeve is characterized by microsegregation that causes solute enrichment in the residual melt. This melt ends up precipitating extensive cell boundary carbides upon solidification and may also cause density segregation due to the centrifugal force [14, 15]. The commercial HT can partly dissolve some of the soluble carbides, however, the cell boundary carbide networks cannot be broken. HT is especially conducted to (1) effectively transform the soft retained austenite (RA) to hard martensite, (2) temper the martensite to increase its toughness, and (3) increase the hot hardness of the martensitic matrix through secondary precipitation of finely distributed carbides [16]. Therefore, the roll's microstructure is often characterized by local inhomogeneities, particularly those caused by the preferential distribution of eutectic carbides at the cell boundaries. This badly affects the roll's mechanical response.

The ultimate purpose of this study is to establish the extent of the influence of niobium on the hot hardness of the HSS roll, which generally translates to its wear resistance. This study employs a comparative approach in which two HSS roll alloys that differ in the content of niobium are characterized with respect to their solidification behaviors, resulting microstructures and the evolution of the microstructures and hardness with heat treatment.

Experimental Procedure

Predictions of the Solidification Behavior

The solidification of the casted alloys was simulated by the Scheil's partial equilibrium approximation. Scheil's partial equilibrium approximation assumes no diffusion for substitutional elements and infinite diffusion for interstitial elements (C, N, B, H) in the solid and complete diffusion in the liquid [17]. This means that the new eutectic reactions only occur in the residual melt that is progressively enriched with substitutional elements. The required thermodynamic data were generated by the ThermoCalc software using TCFE12-MOBFE7 database.

Materials and Heat Treatment

Two HSS sleeves of dimensions: ∅620 mm × 2070 mm and 60 mm thickness, whose compositions differ in niobium as shown in Table 1, were fabricated by the industrial-scale horizontal centrifugal casting technique. The heats were prepared by melting pig iron in the mains frequency induction furnace overnight followed by additions of ferroalloys, viz., high carbon ferrochromium, ferrovanadium, ferromolybdenun, ferroniobium, ferrotungsten and additions of nickel, manganese, and silicon.

A set of seven radial specimens were extracted from each sleeve. Figure 1 depicts the specimens with dimensions approximately 13 mm × 13 mm cut to standard metallographic size by the Xenon ActSpark electro-discharge

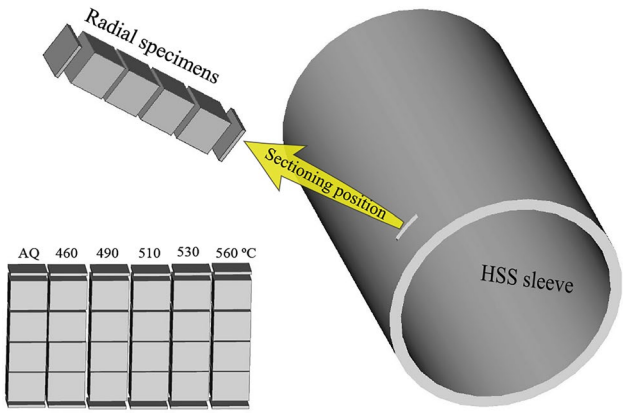

Fig. 1 Schematic diagram of the sampling of the study sleeves

Table 1 Ranges of the chemical composition of the HSS study sleeves

Sleeve/alloy	C	Cr	V	Nb	Mo	W	Mn	Si	Ni
V-0Nb	1.5–2.5	3–8	4–6	…	2.5-5.5	< 1.5	< 1	< 1	< 1.5
V-2Nb	1.5–2.5	3–8	4-6	< 2	2.5-4.5	< 1.5	< 1	< 1	< 1.5

machine at intervals of 13 mm in the radial direction. The outer and inner surfaces, up to 5 mm thick, were cut off to remove the porous oxidized layer.

One radial specimen was reserved as-cast and six were austenitized at 1050 °C for 3600 s in an electric arc furnace before air cooling to room temperature. One specimen of the six was then left as-quenched (AQ) while the remaining five were tempered twice for 7200 s at each of these temperatures, viz., 460, 490, 510, 530, and 560 °C, respectively. Figure 2 summarizes the laboratory heat treatment (LHT) performed.

Preparation of Specimens for Metallography

Preparation of metallographic specimens was performed according to ASTM E3-11 [18] standard on as-cast and heat-treated specimens.

The specimens were mounted on the Struers Multifast Black Bakelite resin using Opal 410 hot-compression machine set to a temperature of 180 °C and force of 30 kN. The mounting was done such that the exposed surface was perpendicular to the radial direction. The exposed surfaces were further ground with silica carbide sandpapers of gradually decreasing grit sizes in the sequence: 120, 180, 240, 400, 600, 800, and 1200. The grinding was performed manually using the SAPHIR 330 machine, applying moderate pressure on the specimens and grinding perpendicular to the previous grinding direction until the existing grinding marks disappeared. The required final surface finish was achieved by progressively polishing with the 3- and 1-µm diamond paste and 0.045 µm colloidal silica using the Struers interpol automatic machine and polishing cloths. The grinding and polishing were performed at a rotational speed of 300 and 150 rpm, respectively. Four major phases were targeted in the microstructures. Therefore, the two etching reagents, including 4% Nital (4% HNO_3 in ethanol) and Groesbeck's reagent (4g $KMnO_4$ + 4g $NaOH_3$ + 100 ml H_2O) were sufficient to reveal the different phases under the OM. The etching was conducted according to ASTM E407-07 standard

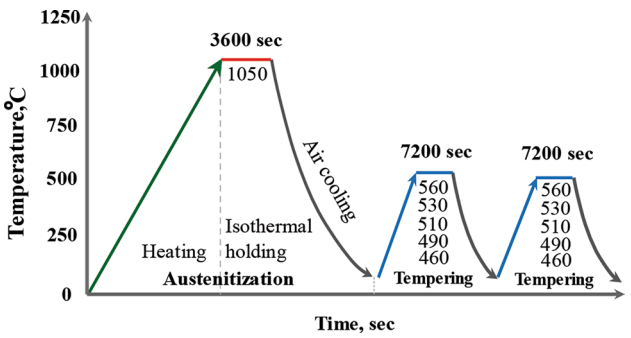

Fig. 2 Schematic diagram of the laboratory heat treatment of HSS roll specimens

[19]. Nital etching was used to darken the martensite while tinting with Groesbeck's reagent was used to discriminate between the three carbides. As for Nital, the etching time depended on the content of RA in the matrix. As-cast specimens had higher RA content and required up to 180 seconds whereas HT specimens required a few seconds.

Microstructural Examination

The OM and SEM were used to examine the microstructures. The Olympus BX51 OM was used for microstructural observation on etched specimens. The OM method was especially conducted to observe microstructural evolution with HT and for carbide volume fractions measurements, in accordance with ASTM E1245-03 standard [20]. For statistical purposes, at least 10 fields of view were captured at 200× magnification on each analyzed surface. The measurements of the content of carbide were performed as a function of the radial depth.

The MIPAR image processing and analysis software was used to measure the carbide volume fractions. The MIPAR software also enabled semi-quantitative measurement of the particle size and spatial distribution of carbides in terms of the major axis length (MAL) and nearest neighbor distance (NND), as described in the literature [21].

The Zeiss Crossbeam 540 field emission gun scanning electron microscope (FEGSEM), integrated with the energy dispersive spectroscopy EDS (EDX) detector was used for higher resolution observations and analysis of the chemical compositions of phases. The SEM was operated at 20 kV accelerating voltage. The SEM system was complemented with the Aztec EDS analysis software, which had different EDS scanning functionalities including point, area, and line scans and area mapping. Area scans were used to average the compositions of the MC eutectic carbide. At least ten different particles for each carbide were analyzed or ten positions of the matrix were scanned. Area mapping was intended for microsegregation analysis and distribution of the MC carbide.

Hardness Measurements

The Future Fv-700 semi-automatic Vickers hardness tester was used to measure the bulk hardness and microhardness under 30 kg and 500 g loads, respectively, according to EN ISO 6507-1:2023 standard [22]. The hardness values were simultaneously converted to Rockwell C (HRC) scale. The tester was operated at room temperature with a dwell time of 10 seconds. The specimens were mounted in Bakelite resin after each HT and prepared by grinding and polishing. A grid was drawn on the surface in steps of 2 mm, avoiding cracks along the edges and in the interior. The bulk hardness was measured on polished surfaces of all specimens

perpendicular to the radial direction after each HT stage. Averages of at least 10 indentations were taken.

Results

The Influence of Niobium on the Solidification Behavior

Figure 3 shows simulations of the solidification behaviors of the two alloys. The predicted carbides are MC, M_7C_3 and M_2C. Their solidification sequence is in the order: $\gamma_{Fe} \rightarrow MC \rightarrow M_7C_3 \rightarrow M_2C$. A notable change observed with Nb addition is the appearance of the proeutectic Nb-rich MC carbide, which begins at a higher temperature. The onset of the V-rich MC carbide is also lifted upwards as the NbC, with a lower Gibbs free energy than VC [11, 23], is precipitated first. Out of a total of 7 wt.% MC carbide that is precipitated, about 1.6 wt.% of the Nb-rich MC is precipitated via the proeutectic reaction.

A comparison can be drawn between the weight fractions of the eutectic carbides obtained for the two alloys, which can be read at the end of each simulation curve. As shown in Fig. 3b, the MC carbide increases after Nb addition due to precipitation of NbC than when only VC forms (Fig. 3a).

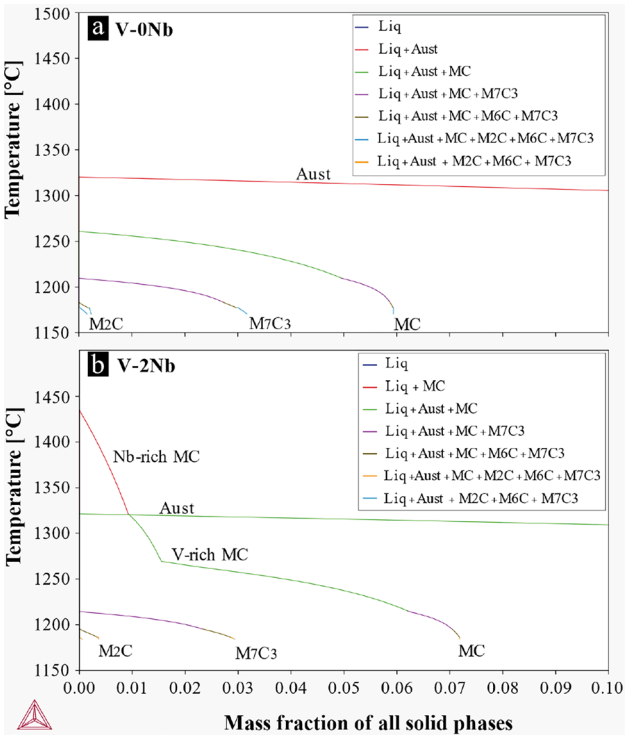

Fig. 3 Scheil's partial equilibrium simulations of the solidification behavior for the two experimental HSS alloys

Figure 4 summarizes the solidification ranges of the two alloys. Note that the MC carbide precipitates over a wide temperature range whereas the Cr- and Mo-rich carbides precipitate near the end of solidification over a short range from the depleting and highly enriched residual melt. Their solidification range of Cr- and Mo-rich carbides is also shortened and lifted by niobium addition. The calculated liquidus and solidus temperatures are 1317 and 1168 °C for V-0Nb, and 1327 and 1188 °C for V-2Nb, respectively.

Phases in the HSS Microstructures

Figure 5 shows a typical microstructure in as-cast condition after etching with 4%Nital. The microstructure comprises a mixture of martensite, RA, and eutectic carbides.

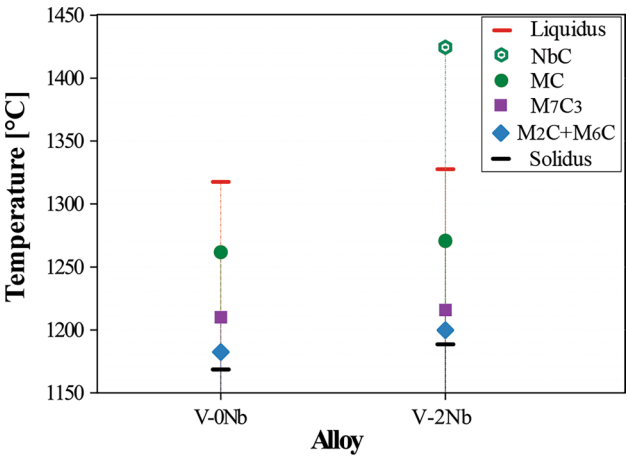

Fig. 4 Summary of the predicted solidification ranges of the experimental HSS alloys

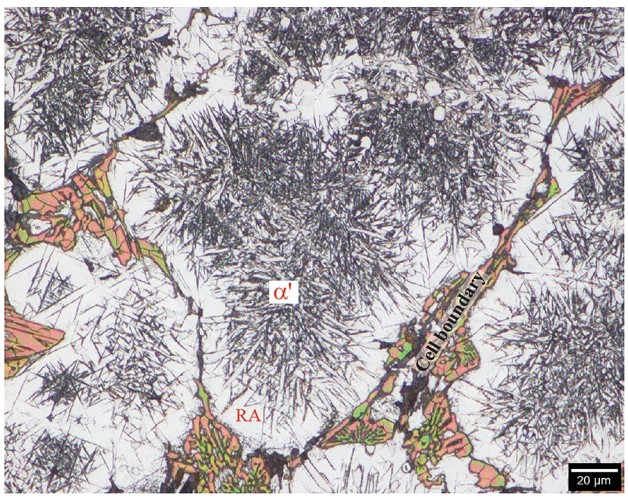

Fig. 5 Optical micrographs of as-cast microstructure showing the distribution of RA relative to martensite (**a'**); etched with 4% Nital and Groesbeck's

The martensite is concentrated in the inner regions of the solidification cells whereas the cell border (periphery) shows a strong presence of RA. The martensite occurs as thin, randomly oriented plates. Martensite etches dark with Nital, and RA appears white as it is stubborn to etching. Many smaller plates intersect with each other or carbide particles. Some zigzag patterns can also be observed, as evidence of autocatalysis. The eutectic carbides include the V/Nb-rich MC, Cr-rich M_7C_3, and the Mo-rich M_2C.

Figure 6 shows as-cast the typical difference between the microstructures of the two sleeves extracted from a radial depth between 20 and 30 mm and etched with Groesbeck's reagent. Only the distribution and particle size of the eutectic and submicron-size secondary carbides were revealed whereas the martensitic matrix is untainted. The M_7C_3 is colored in a rainbow color range and occurs along the cell boundaries. The dark-brown, acicular carbide on the cell boundary is the M_2C. The eutectic MC and submicron carbide particles are outlined.

The effect of niobium addition on the particle size, morphology, and distribution of the MC carbide is apparent. V-0Nb consists of idiomorphic and petal-like/chicken-feet-like MC carbide, as they have been described in the literature [10, 13]. V-2Nb contains mainly agglomerated MC carbide particles. The MC carbide morphologies also vary with radial depth; it will be shown later that specific morphologies are prevalent at specific depths.

In V-0Nb (Fig. 6a), the MC carbide particles are large; almost all the MC carbide particles occur on cell boundaries, with a large area in the interior of the solidification cell without eutectic carbide. Many particles have petal-like or chicken-feet-like morphologies, found at triple points. The MC carbide can be seen joining up with the M_7C_3 carbide along the cell boundaries.

In V-2Nb, the MC carbide forms agglomerates (circled in Fig. 6b) and irregular particles; the eutectic MC carbide is not easily traceable along the cell boundaries. Note the MC carbide is partially tainted when Nb is added; this effect is caused by impurity species, as will be shown later with the EDS data. The submicron carbide particles appear coarser, more densely distributed, and dispersed in V-2Nb than in V-0Nb, with the precipitate-free-zone (PFZ) clearly visible in V-0Nb.

Volume Fraction of Carbides

Figure 7 shows the variations in carbide volume fraction as a function of depth for the microstructures tempered at a peak temperature of 530 °C. Both V-0Nb and V-2Nb show a high content of the M_7C_3 carbide near the outer and inner surfaces of the radial section. Furthermore, at these two positions, the two sleeves also show a small difference between the volume

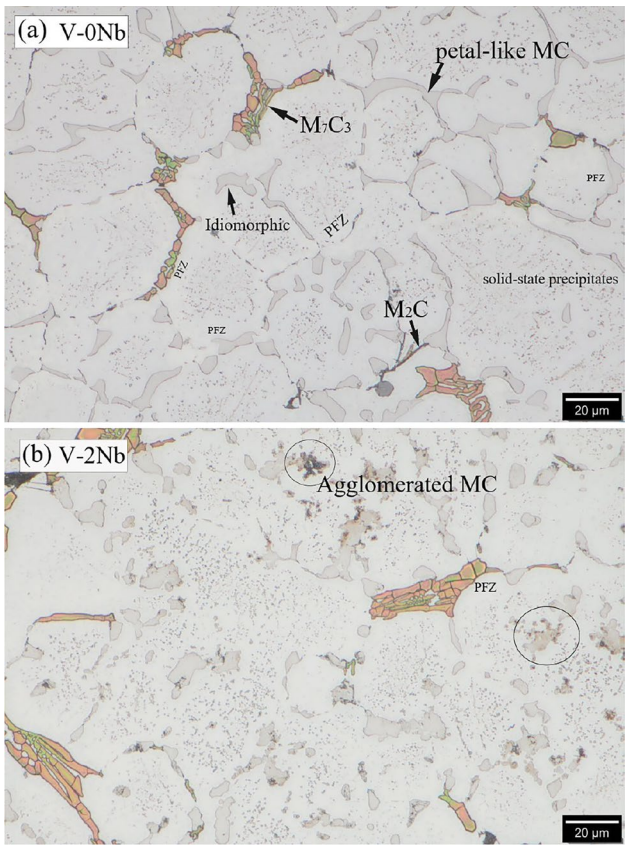

Fig. 6 Optical micrographs of as-cast microstructures extracted at a radial depth between 20 and 30 mm for the (**a**) V-0Nb and (**b**) V-2Nb sleeves. Groesbeck's etched

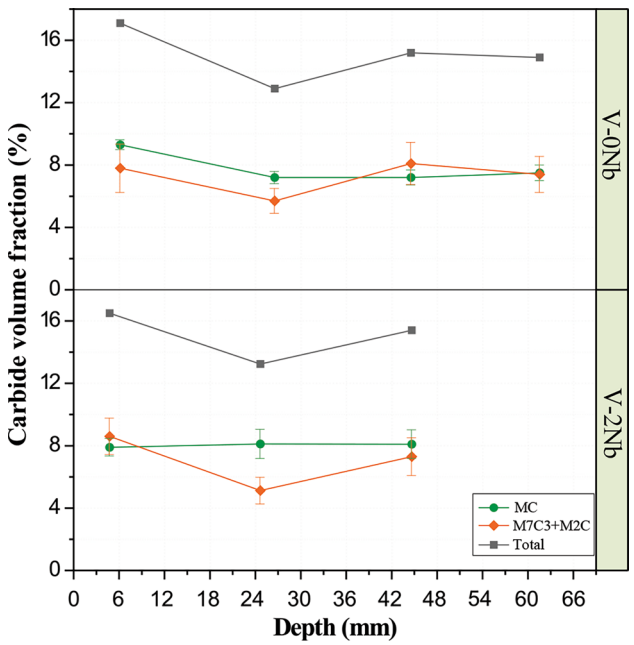

Fig. 7 Variation in carbide content as a function of depth

fractions of the MC and M_7C_3 carbides. The MC carbide own generally shows little variation with depth.

Qualitative analysis of the distributions and morphologies of carbides across depth

The micrographs in Fig. 8 represent microstructural variations with radial depth for the two sleeves. These variations are comparable to the carbide content variations shown in Fig. 7. In these micrographs, a combination of etchants (Nital then Groesbeck's) was employed to examine the particle sizes and spatial distribution of the MC and M_7C_3 carbides. In the outer 10 mm, the two microstructures are nearly similar (Fig. 8a & b). They show evidence of a high cooling rate whereby the redistribution coefficients of alloying elements were near unity [24]; not much microsegregation

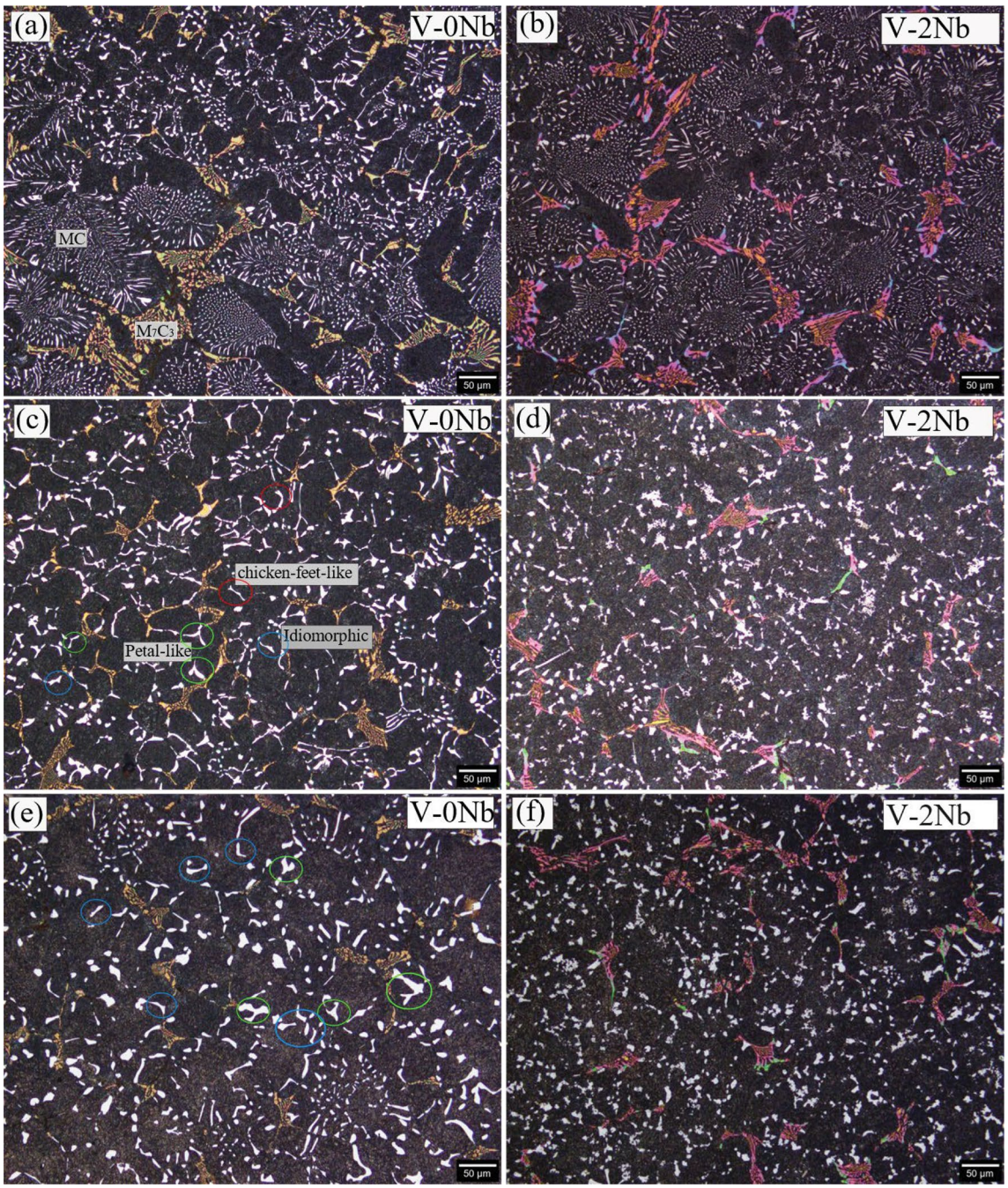

Fig. 8 Optical micrographs of the tempered microstructures at 0–10 mm depth (**a** and **b**), 20–30 mm depth (**c** and **d**), and 40–50 mm depth (**e** and **f**)

occurred in the residual melt because the undercooling was relatively large, and the solidification rate was rapid.

This is exhibited by the fine spherical MC carbide in the center of the solidification cell, followed by the fine rod-like MC carbide radiating out. Nonetheless, the outer 10 mm of the sleeve is ultimately oxidized during HT and eventually removed by machining. The reader may also notice the color variations in the micrographs, which is an artefact due to variations in the etching time. In the middle of the radial section, the difference between the two sleeves is pronounced. Between 20 to 30 mm, V-0Nb has nearly all the MC carbide on cell boundaries (Fig. 8c). The MC carbide morphologies include the idiomorphic, found on the boundaries between two solidification cells, and petal-like or chicken-feet-like morphologies found at triple points. In contrast, V-2Nb contains dispersed, irregular, agglomerated and granular MC carbide that is completely untraceable to the cell boundaries (Fig. 8d). Between 40 and 50 mm, V-0Nb largely contains coarse idiomorphic, petal-like, elliptical and rod-like MC carbide (Fig. 8e). Some elliptical and rod-like particles are located within the matrix while the petal-like and idiomorphic occur on cell boundaries. V-2Nb still contains irregular, agglomerated, and granular MC carbide that is fully dispersed (Fig. 8f). Table 2 summarizes the variations in the distributions and morphological features of the MC carbide observed in the two sleeves. The through-thickness distribution of the MC carbide indicates that significant particle refinement and dispersion were achieved by niobium addition.

Quantitative Analysis of the Distribution of Carbides

Figure 9 shows the variations in the MC carbide particle sizes (MAL) and spatial distributions NND as functions of depth. The results indicate a substantial size and spatial distribution variability (very large error bars). The first 10 mm shows the smallest MAL and NND, which reflects the strong influence of the cooling rate as observed in Fig. 8a & b. Both V-0Nb (solid black lines) and V-2Nb (dashed red lines) contained much finer eutectic MC particles, with average MAL and NND values of between 3 and 4 µm. The

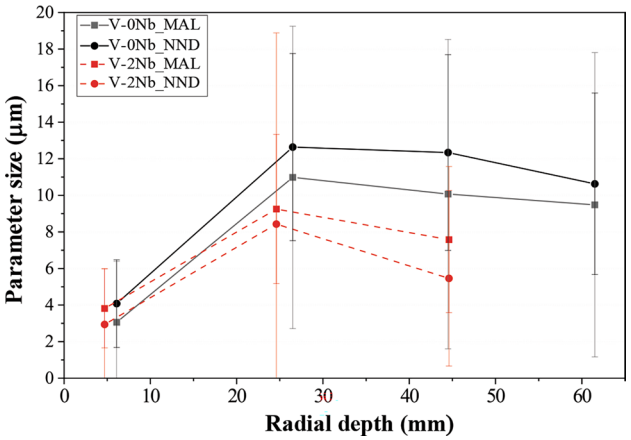

Fig. 9 Variations in the average particle size (MAL) and spatial distribution (NND) of the MC carbides as functions of depth for the two sleeves

MAL and NND generally reached their peaks somewhere in the middle of the radial section. Both V-0Nb and V-2Nb showed clearer peaks between the depth of 25 and 30 mm. For V-0Nb, the MAL and NND were much higher than 10 µm, which suggests the coarser particles that are further apart. In contrast, the MAL and NND values for V-2Nb were lower than 10 µm, which suggests refined particles that are close to each other.

The Compositions of the MC Carbide

The chemical compositions of the MC carbide are shown in Table 3. The V content of the MC carbide decreases with Nb addition as depicted in Fig. 10. In V-0Nb the content of V in the MC is high as expected because this sleeve did not contain Nb as a strong MC former in solid solution. In V-2Nb, the content of V in the MC carbide decreased by over 24 wt.%. This observation suggests that Nb addition in the alloy decreases the solid solubility of vanadium in the MC crystal structure during solidification. Figure 11 shows the elemental maps of tempered microstructures of the two sleeves. The distribution of the MC carbide can again be

Table 2 Depth dependence of the morphology and distribution of the MC carbide

Depth, mm		V-0Nb	V-2Nb
0–10	Morphology	spherical, rod-like	Spherical, rod-like
	Distribution	Homogeneous, mainly cell interiors, dispersed	Homogeneous, mainly cell interiors, fully dispersed
20–30	Morphology	Idiomorphic, petal- & chicken-feet- like	Granular, irregular, agglomerated
	Distribution	Cell boundaries	Homogeneous, fully dispersed
40–50	Morphology	elliptical, idiomorphic, petal- & chicken-feet-like	Granular, irregular, agglomerated,
	Distribution	largely on cell boundaries	Homogeneous, fully dispersed

Table 3 Statistical EDS data of the MC for the two sleeves after tempering twice at 530 °C (wt.%)

HT	Sleeve	Statistic	Fe	Cr	V	Nb	Mo	W	Trace
T2-530	V-0Nb	Mean	3.0	5.6	66.6	0.5	10.0	8.3	6.0
		Min	2.0	3.7	40.4	0.3	4.2	4.3	1.0
		Max	4.1	6.5	63.9	0.6	18.9	10.7	7.0
		Std	0.7	1.0	7.1	0.1	4.5	2.1	2.0
		CV	22.5	18.3	10.6	24.1	44.7	24.6	33.0
		95% CI	0.4	0.6	4.1	0.1	2.6	1.2	1.0
		Ra	13.1	10.6	6.1	14.0	25.9	14.3	19.0
T2-530	V-2Nb	Mean	4.5	5.2	42.5	20.3	9.9	7.8	10.0
		Min	2.7	3.6	28.1	5.6	6.8	4.6	4.0
		Max	10.7	11.3	61.8	30.6	17.2	15.9	35.0
		Std	2.3	2.2	7.1	8.5	3.7	3.1	9.0
		CV	51.9	41.4	16.7	41.8	37.2	39.5	94.0
		95%CI	1.9	1.7	5.6	4.9	2.7	1.5	5.0
		Ra	41.1	32.8	13.3	24.2	27.3	18.7	54.0

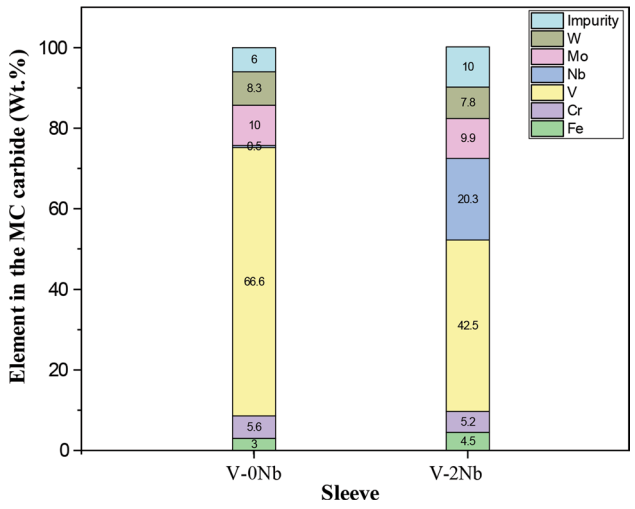

Fig. 10 Effect of Nb addition on the content of vanadium in the MC eutectic carbide

traced by the elemental intensity distribution of Nb and V. V-0Nb only shows the high intensity of V on the cell boundary (Fig. 11a-c). In contrast, in V-2Nb (Fig. 11d-h) the intensities of V, Nb, and Mo, which are the main components of the MC carbide, can be seen dispersed in lumps, i.e., there is no preferential cell boundary distribution of this carbide. It can again be seen that Nb and V homogenized through diffusion within the MC carbide as the solidification progressed, so that they distributed similarly.

Influence of Niobium Addition on Hardness During Tempering Treatment

Figure 12 shows the hardness curves for both the first and second tempering heat treatments. Both V-0Nb and V-2Nb had similar as-quench hardness values of about 60.2 and 60.3 HRC. The as-quench hardness only reflected the small amount of martensite formed after air cooling since a small amount of RA transformed into hard martensite. Tempering at 460 °C for 7200 seconds had little effect on the hardness of the sleeves, even after the second tempering treatment due to the slower diffusivity of the alloying elements given the short laboratory heat treatment timescales. However, after first tempering at 490 °C, the hardness increased dramatically and kept improving, reaching a peak at 530 °C. Both sleeves continued to show high hardness values after the first tempering treatment since a large quantity of fresh martensite that formed was not sufficiently tempered. However, after the second tempering treatment, the hardness of the V-0Nb sleeve dropped below its first temper hardness meanwhile the V-2Nb sleeve remained relatively uniform. Their bulk hardness values after the second tempering treatment were rather equal at 64 HRC.

Figure 13 shows the second temper bulk and matrix hardness as functions of radial depth, investigated for the influence of density segregation. The matrix hardness was higher than the bulk hardness, which is consistent with the previous report [25], and shows some fluctuations within one HRC. A small peak occurs between 15- and 20-mm depth, where the lowest carbide content was obtained. (Fig. 7). The higher radial hardness values obtained for the matrix are explained through an illustration in Fig. 14. It can be seen that indenting with a large load (30 kg) on both the matrix and carbides resulted in cracking due to large brittle carbides and rotation of small spherical carbide particles (Fig. 14a & b). This significantly led to lower bulk hardness than would be obtained if carbides did not crack or rotate. In comparison, indenting only the matrix resulted in no cracks, Fig. 14c & d, whereby the full resistance of the matrix to deformation

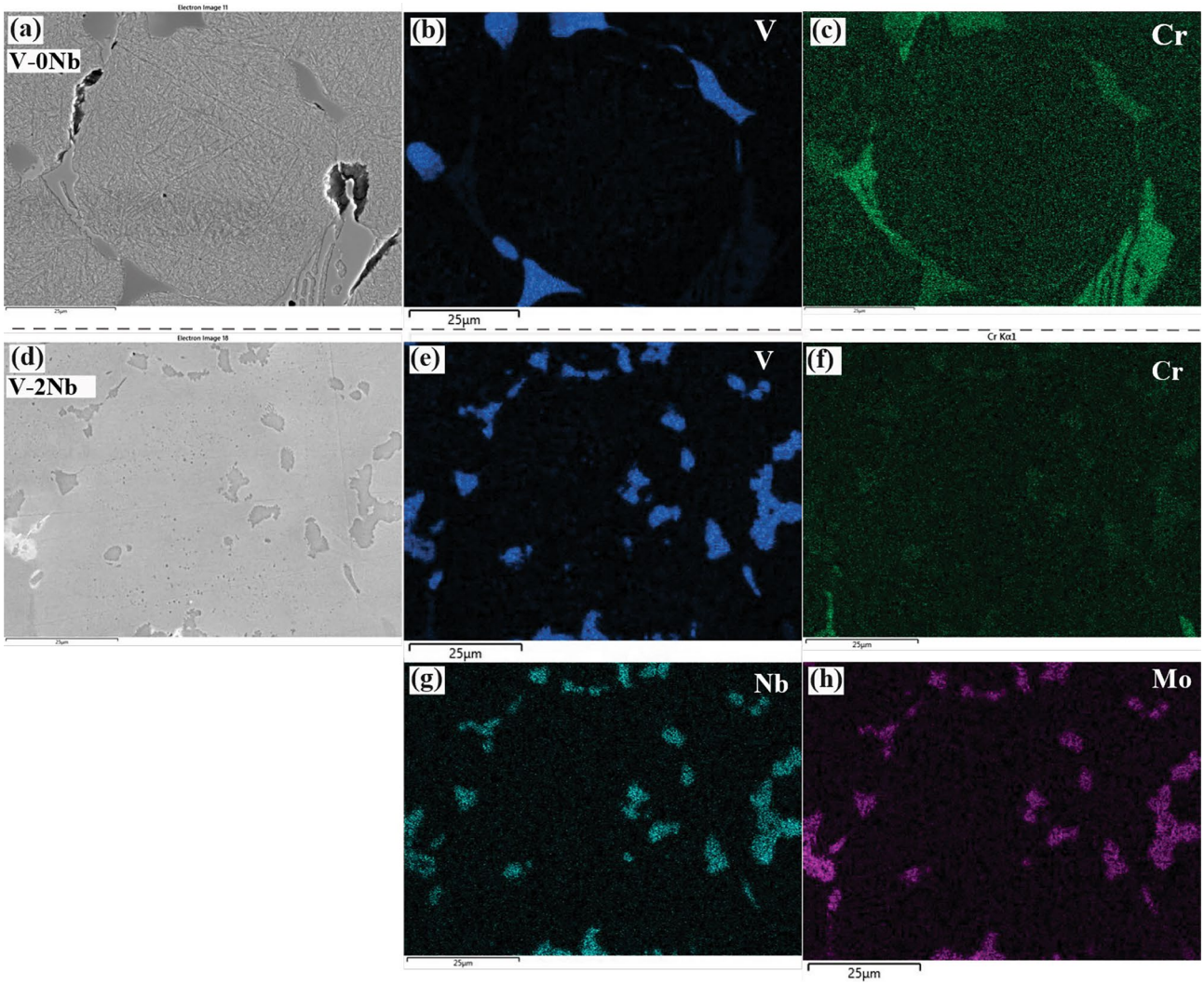

Fig. 11 EDS area map of the tempered microstructure of V-0Nb (**a**–**c**) and V-2Nb (**d**–**h**)

was in effect. Nonetheless, it is worth noting that carbides are very important in that they are refractories whereas the matrix is not. Thus, carbides stabilize the matrix through temper resistance, thereby increasing resistance to abrasive wear during hot-rolling.

Both sleeves exhibited a trough-like radial hardness, which reflects the volume fractions, particle size and distribution of carbides described in Sections "Phases in the HSS microstructures" and 3.3. The inner and outer extremes of the section had a higher hardness since they had high carbide volume fractions. The hardness difference was not significant at room temperature as seen by the error bars. However, V-2Nb exhibited a higher and shallower trough than V-0Nb by virtue of better carbide particle dispersion and refinement.

Discussion

Effect of Solidification on the Distribution of Carbides

Figure 15 depicts the general evolution of the two microstructures during solidification as observed with the microscopy. The MC carbide in V-0Nb occurs mainly on cell boundaries. Accordingly, V-0Nb started to precipitate the MC carbide after a long event of vanadium enrichment in the residual melt. This is because this alloy does not precipitate NbC, which should lift the precipitation temperature of the MC carbide since it has a lower Gibbs free energy than VC. Therefore, the MC was only precipitated

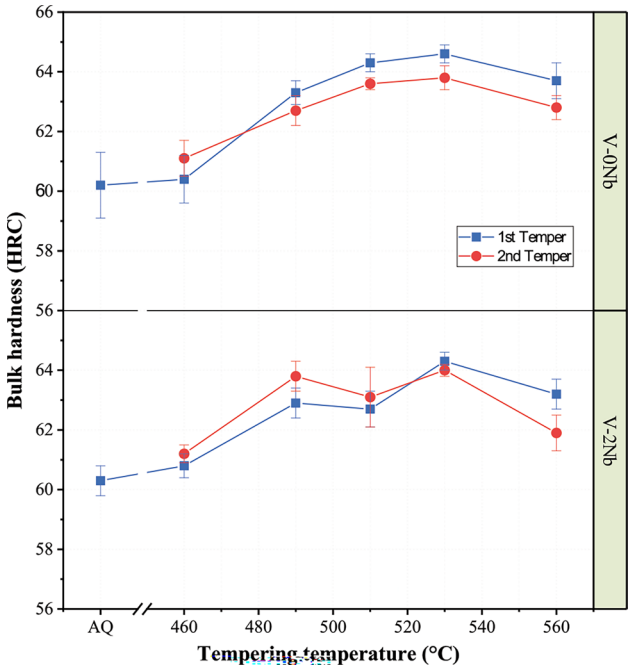

Fig. 12 Bulk hardness (HRC) variations with tempering temperature averaged across the radial thickness

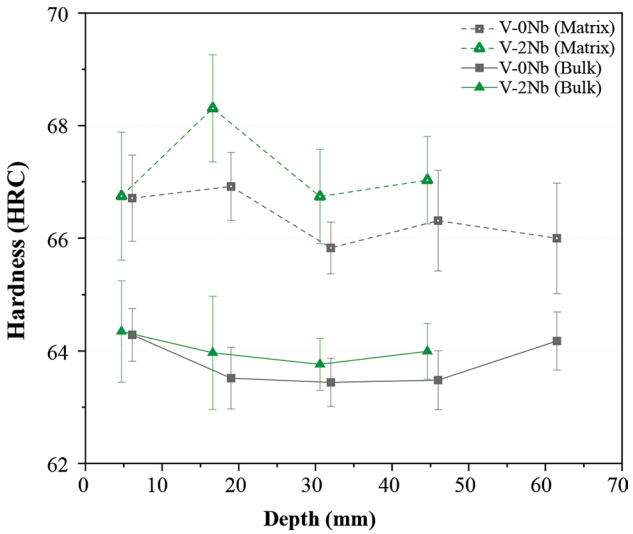

Fig. 13 Bulk hardness (HRC) variations with radial depth for the two microstructures tempered twice at 530 °C

at a lower temperature, toward the end of austenite crystallization and on cell boundaries. When precipitated at triple points of the solidification cells, the MC carbide particles formed petal-like or chicken-feet-like morphologies and those on linear boundaries became idiomorphic (Fig. 6a & 9a).

However, with niobium addition in V-2Nb no prior enrichment was required as the proeutectic Nb-rich MC had already precipitated in the melt. The microstructure also suggests no new independent nucleation of the V-rich MC eutectic carbide as shown by the EDS mapping in Fig. 12 indicating V and Nb occurring together in the MC carbide. Rather, when vanadium eventually became supersaturated, the already formed Nb-rich proeutectic MC carbide continued to grow epitaxially from this supersaturation since their lattice constants were similar [26].

Influence of Heat Treatment

The hardness improved due to the formation of additional martensite from RA through repeated tempering treatments. The hardness did not significantly change when tempering at 460 °C. This suggests insufficient diffusion of carbon out of solution of austenite, which is confirmed by the small change in hardness from the as-quench condition, Fig. 12. In other words, the tempering led to more stabilization of austenite.

However, the hardness increased substantially after tempering at temperatures above 490 °C, reaching a peak at 530 °C, which corresponded to the maximum volume fraction of martensite. At 560 °C the hardness started dropping due to over-tempering; in which case the martensite and RA rapidly decomposed to ferrite.

The matrix hardness obtained was exceptionally high after tempering twice (Fig. 13), and this is because the matrix does not crack during indentation as explained in section "Influence of niobium addition on hardness during tempering treatment". Such high matrix hardness suggests that the toughness can still be increased further by prolonging the tempering treatment without seriously lowering the hot hardness as is the case for commercial HT of rolls.

It can be seen again that during the second tempering treatment, the effect of temper softening resistance took effect. For example, V-0Nb showed a notable drop in the second temper hardness due to its poor carbide distribution, suggesting that the microstructure developed during the initial tempering had less temper resistance. The opposite was true for V-2Nb, as observed earlier, the MC carbide particles were refined and dispersed (Figures 8(b) and 9(b)). Thus, the particle size refinement and full dispersion of the eutectic MC carbides that occurred during solidification had a greater influence due to the smaller MAL and proximity (smaller NND) among the carbide particles in V-2Nd (Fig. 10).

Influence of Microstructure on Hardness

There is a difference in the hardness between the two sleeves, which is owed to the distributions of the MC carbide (Fig. 8). However, the variations with depth are similar. The matrix hardness shows a small variation and a peak between 15- and 20-mm depth, where it is notably high.

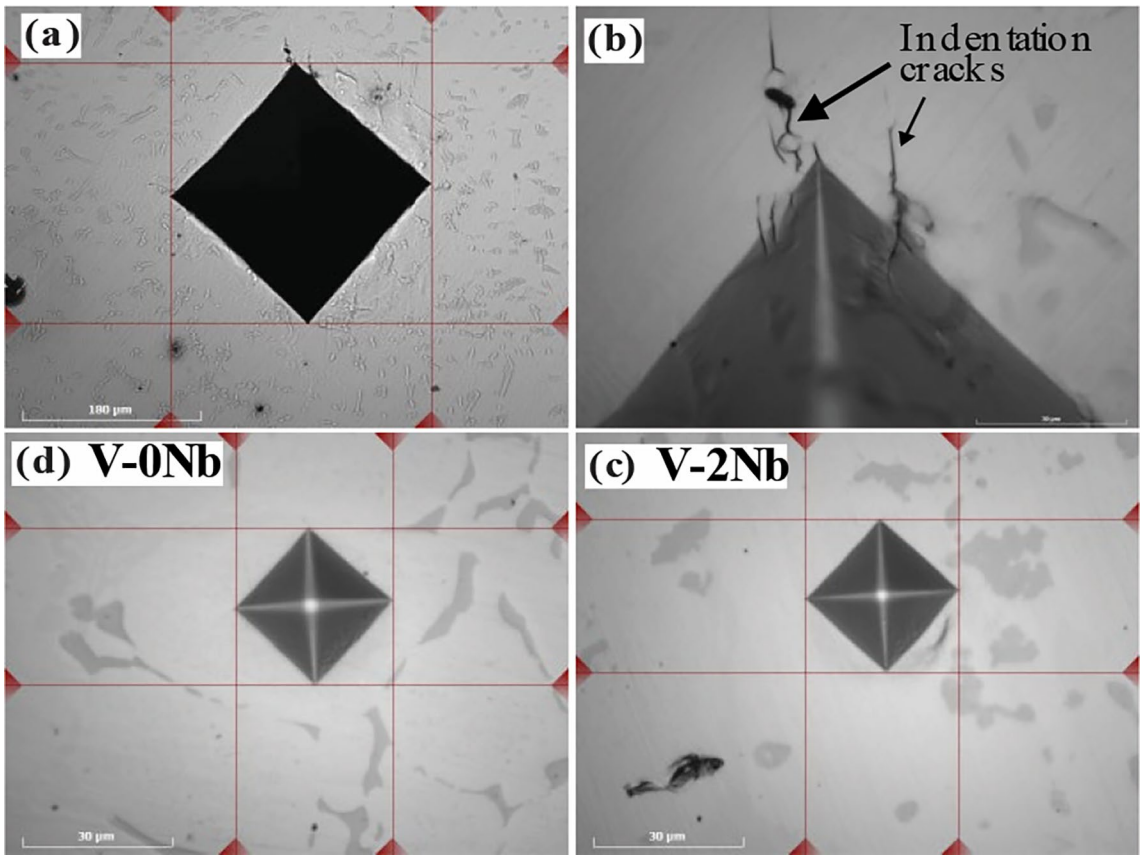

Fig. 14 Vickers hardness indentations of the specimens: (**a**) HV30, (**b**) higher magnification HV30, and (**c** and **d**) HV0.5

The high matrix hardness at this depth suggests an inverse relationship to the carbide volume fraction since the carbide volume fraction was minimal. This could be due to a harder martensite forming from a higher carbon content than the other positions since the lowest carbide content (carbon sink) was precipitated at this depth (Fig. 7). The bulk hardness depended largely on the carbide content, showing high values at positions of high carbide volume fractions. Both the radial carbide contents and bulk hardness show a trough distribution, which is evidence of density segregation, which notably affected the first 20 mm from the surface of the sleeve.

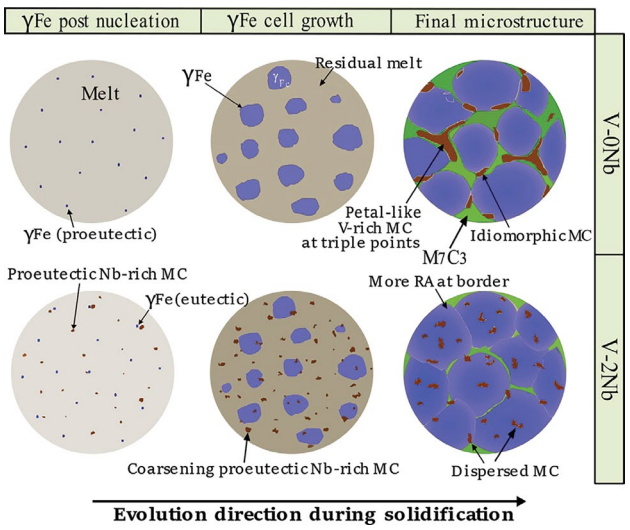

Fig. 15 Schematic diagram illustrating the evolution and distribution of the MC carbide as it precipitates with austenite (γFe) for each sleeve as observed in the as-cast microstructures.

The overlap of the hardness error bars indicates that the two sleeves achieved the same hardness. However, it was shown that owing to the microstructural differences, the two alloys responded differently to the HT. Furthermore, an important factor to consider is the effect of the LHT on the degree of temper softening of the sleeves, which in this context, was a function of the secondary hardening by carbides. Given the short timescale of the LHT, it is apparent that the improved dispersion of eutectic carbide could not be fully leveraged to retard the temper softening of the sleeves. In other words, under typical roll production HT conditions, the V-2Nb alloy will emerge superior after the martensite is fully tempered. Furthermore, when the rolls are in use in the HSM, both the carbide dispersion and secondary precipitates are critical in retarding temper softening. Hence,

these results suggest that the V-0Nb alloy can significantly deteriorate much quicker than V-2Nb over time.

Conclusions

A study was conducted on the centrifugal-cast sleeve of the commercial HSS roll to establish the effects of niobium addition on the solidification behavior and response to HT, and how they correlate to the hardness. This study concludes that the two alloys responded differently to the HT due to their difference in the particle size and dispersion of the MC carbide. The addition of approximately 2 wt.% Nb in the HSS roll alloy promotes the precipitation of sufficient Nb-rich proeutectic MC carbide to caused refinement and dispersion of the MC carbide in the microstructure which improved the microhardness of the martensitic matrix. The dispersed MC carbide counteracted softening during repeated tempering treatment, helping the microstructure retain the high hardness of the roll. The hardness of the matrix is significantly high after tempering twice using LHT suggesting that a sufficiently high hardness can be maintained after prolonged industrial HT. Therefore, it can be concluded that Nb-containing HSS roll exhibited better microstructural integrity for improved hot hardness. In other words, Nb-containing HSS rolls can be produced for the hot-rolling stands that operate at higher rolling force and temperature if the cost-benefit analysis is favorable.

Acknowledgements The authors of this paper wish to thank the South African Roll Company for both the technical and financial support and the University of Pretoria for the research facilities.

Funding Open access funding provided by University of Pretoria.

References

1. R. Kurahashi, Development and application of high-speed tool steel rolls in hot strip rolling. Nippon Steel Technical Report. 66(0) (1995). UDC621.771.23:669.14.018.251.9
2. E. Kerr, R. Webber, D. McCaw, Roll performance-technical overview and future outlook. Ironmak. Steelmak. **31**(4), 295–299 (2004). https://doi.org/10.1179/030192304225018172
3. V.M. Kolokoltsev, N.A. Feoktistov, A.S. Savinov, E.V. Skripkin, Development of new composition for sHSS steel used for hot rolling mill rolls at Magnitogorsk iron and steel works. CIS Iron and Steel Rev. **23**, 24–27 (2022). https://doi.org/10.17580/cisisr.2022.01.05
4. J.W. Park, H.C. Lee, S. Lee, Composition, microstructure, hardness, and wear properties of high-speed steel rolls. Mater. Trans. A. **30**(2), 399–409 (1999). https://doi.org/10.1007/s11661-999-0329-9
5. M. Pellizzari, A. Molinari, G. Straffelini, Tribological behaviour of hot rolling rolls. Wear. **259**(7–12), 1281–1289 (2005). https://doi.org/10.1016/j.wear.2004.12.006
6. S.W. Kim, U.J. Lee, K.D. Woo, D.K. Kim, Solidification microstructures and mechanical properties of vertical centrifugal cast high speed steel. Mater. Sci. Tech. **19**(12), 1727–1732 (2003). https://doi.org/10.1179/026708303225008356
7. A. Molinari, A. Tremea, M. Pellizzari, A. Biggi, G. Corbo, High speed steels for hot rolls with improved impact and thermal fatigue resistance. Mater. Sci. Tech. **18**(12), 1574–1580 (2002). https://doi.org/10.1179/026708302225007664
8. Y.J. Kang, J.C. Oh, H.C. Lee, S. Lee, Effects of carbon and chromium additions on the wear resistance and surface roughness of cast high-speed steel rolls. Metal. Mater. Trans. A. **32**(10), 2515–2525 (2001). https://doi.org/10.1007/s11661-001-0041-x
9. H.G. Fu, J.D. Xing, A fundamental research of electromagnetic centrifugal cast high speed steel (HSS) roll. Steel Res. Int. **78**(3), 266–272 (2007). https://doi.org/10.1002/srin.200705890
10. Y. Luan, N. Song, Y. Bai, X. Kang, D. Li, Effect of solidification rate on the morphology and distribution of eutectic carbides in centrifugal casting high-speed steel rolls. J. Mater. Proc. Tech. **210**, 536–541 (2010). https://doi.org/10.1016/j.jmatprotec.2009.10.017
11. J.R.C. Guimeraes, *Report on Tool Steel Developments* (CBMM, Sao Paolo, 1986)
12. H.J.I.L.Z. Veliko, V. Kroma, Thermodynamic modeling for the alloy design of high speed steels and high chromium cast irons. Mater. Tech. **44**(3), 121–127 (2010)
13. H. Wang, L. Hou, J. Zhang, L. Lu, H. Cui, J. Zhang, The secondary precipitates of niobium-alloyed M3:2 high speed steel prepared by spray deposition. Mater Charact. **106**, 245–254 (2015). https://doi.org/10.1016/j.matchar.2015.06.006
14. Y.K. Luan, N.N. Song, Y.L. Bai, X.H. Kang, D.Z. Li, A segregative MC carbide in centrifugal casting high speed steel roll. Adv. Mater. Res. **154**, 269–272 (2010). https://doi.org/10.4028/www.scientific.net/AMR.154-155.269
15. T. Koseki, *Recent activities in research of casting* (Kawasaki Steel Technical Report-English Edition, 1999), pp.67–69
16. H. Fu, Y. Qu, J. Xing, X. Zhi, Z. Jiang, M. Li, Y. Zhang, Investigations on heat treatment of a high-speed steel roll. J. Mater. Eng. Perform. **17**, 535–542 (2008). https://doi.org/10.1007/s11665-007-9174-4
17. H. Zhang, C.A. Gandin, J. He, K. Nakajima, Prediction of solidification path and carbide precipitation in Fe–C–V–Cr–Mo–W high speed steels, in *IOP Conference Series: Materials Science and Engineering* (IOP Publishing, 2012), p. 012061. https://doi.org/10.1088/1757-899X/33/1/012061
18. ASTM E3-11, *Standard Guide for Preparation of Metallographic Specimens* (ASTM International, West Conshohocken, 2017)
19. ASTM E407-07, *standard Practice for Microetching Metals and Alloys* (ASTM International, West Conshohocken, 2015)
20. ASTM 1245-03, *Standard Practice for Determining the Inclusion or Second-Phase Constituent Content of Metals by Automatic Image Analysis* (ASTM International, West Conshohocken, 2023)
21. L. De Colnet, E. Pirard, J. Tchoufang Tchuindjang J. Lecomte-Beckers, R. Gfhiri, P. Boeraeve, S. Lescott, Qualitative description

of MC, M_2C, M_6C and M_7C_3 carbides in High speed steel rolls, in *MSMF-3 International conference held in Brno* (ResearchGate, 2001)
22. EN ISO 6507-1, *Metallic Materials. Vickers Hardness Test. Part 1 Test Method* (International Organization for Standarization, London, 2023). www.iso.org
23. S. Karagöz, H.F. Fischmeister, Niobium-alloyed high speed steel by powder metallurgy. Metall. Trans. A. **19**, 1395–1401 (1988). https://doi.org/10.1007/BF02674013
24. R.E. Reed-Hill, R. Abboschian, R. Abbaschian, *Physical Metallurgy Principles*, 4th edn (Van Nostrand, New York, 1973), pp.435–436
25. M. Nilsson, M. Olsson, Microstructural, mechanical and tribological characterisation of roll materials for the finishing stands of the hot strip mill for steel rolling. Wear. **307**(1–2), 209–217 (2013). https://doi.org/10.1016/j.wear.2013.09.002
26. N. Oono, H. Nitta, Y. Lijima, Diffusion of niobium in α-iron. Mat. trans. **44**(10), 2078–2083 (2003). https://doi.org/10.2320/matertrans.44.2078